13th International Conference on
Structural Health Monitoring of Intelligent Infrastructure
DOI: 10.3217/978-3-99161-057-1-157

Full-Scale Bridge Testing: Lessons from the Demolition of the Steinavötn Bridge

Sigurdardottir, Dorotea H[1, 0009-0006-8496-4625], Tsai, Ching-Yi[1, 0000-0002-0122-2575], Guðmundsson, Guðmundur Valur[2]

[1]Faculty of Civil and Environmental Engineering, University of Iceland, Sæmundargötu 2, 102 Reykjavík, Iceland
[2]Division of Development, The Icelandic Road and Coastal Administration, Suðurhraun 3, 210 Garðabær, Iceland
email: dorotea@hi.is, cytsai@hi.is, gudmundur.v.gudmundsson@vegagerdin.is,

ABSTRACT: Structural engineers, particularly bridge engineers, rarely have the opportunity to test full-scale bridges to failure due to the high costs involved. Such experiments are typically conducted on scaled-down specimens in controlled settings, which can introduce challenges in accurately correlating results to real-world full-scale behavior. In 2019, a unique opportunity arose when the Steinavötn bridge in southern Iceland was irreparably damaged by flooding. Built in 1964, the 102-meter-long reinforced concrete continuous beam bridge had two abutments and five piers and was part of Iceland's national road system, connecting the ring road around the island. One of its piers suffered scour damage beyond repair, leading to the decision to demolish the structure. Before its demolition, a measurement campaign was conducted using long-gauge fiber-optic sensors to capture the bridge's response to ultimate loading. This study presents the findings from the measurement campaign and bridge modelling, providing valuable insights into the ultimate load behavior of a full-scale bridge and advancing the understanding of structural performance under extreme conditions.

KEY WORDS: Full-scale testing, Bridge modelling, Continuous beam bridge, Long-gauge fiber-optic sensors, Reinforced concrete.

1 INTRODUCTION

In 2017, a unique opportunity arose when the Steinavötn bridge in southern Iceland was irreparably damaged by flooding. Built in 1964, the 102-meter-long reinforced concrete continuous beam bridge had two abutments and five piers (Figure 1) and was part of Iceland's national road system, connecting the ring road around the island. One of its piers suffered scour damage beyond repair, leading to the decision to demolish the structure. Before its demolition, extensive load testing and vibration measurements were conducted on it during the summer of 2019. These tests were carried out as a collaborative effort involving the Icelandic Road and Coastal Administration (IRCA), Reykjavik University, ETH Zurich, and Osmos Monitoring Group. Various sensors were used during the measurements, including force gauges, displacement sensors, accelerometers, and different types of strain sensors. The bridge response was recorded under various load scenarios, such as excitation from natural environmental vibrations, controlled traffic loads on the bridge, impact loads, and gradually increasing vertical loads on one bridge span far into the non-linear regime.

The events leading up to and the causes of the bridge's destruction have been examined in a master's thesis written at the University of Iceland [1]. A bachelor's thesis at Reykjavik University documented the setup of the load tests on the bridge and the data collection process. It presented results from material tests on concrete and reinforcement steel. Furthermore, preliminary numerical computational models of the bridge were developed, deflections were calculated, and the load-bearing capacity was compared with measurement data as well as with design calculations [2]. The dynamic behavior of the bridge has also been analyzed based on vibration data by a research group at Reykjavik University and the Technical University of Denmark [3], [4]. A comparison between non-linear beam-truss models with different boundary conditions was conducted at the University of Iceland [5].

Structural engineers, particularly bridge engineers, rarely have the opportunity to test full-scale bridges to failure due to the high costs involved. Such experiments are typically conducted on scaled-down specimens in controlled settings, which can introduce challenges in accurately correlating results to real-world full-scale behavior. It is therefore important to seize the opportunity and conduct full-scale experiments to improve knowledge and understanding of structural behavior as well as validating numerical models. Data analysis methods and numerical models developed in these rare settings provide valuable insights into structural behavior, numerical modelling, and structural health monitoring methods.

In this paper insights from data measured by the long-gauge fiber-optic strain sensors and LVDT displacement sensors during the ultimate load test at Steinavötn bridge are presented.

Figure 1. The Steinavötn bridge. Photo from ICRA, 2019.

DOI: 10.3217/978-3-99161-057-1-157

2 THE STEINAVÖTN BRIDGE

2.1 Description of the bridge

The Steinavötn Bridge on National Road 1 was built by the IRCA in 1964 and was located in the Suðursveit region of Southeast Iceland, south of Vatnajökull, about 61 km west of Höfn in Hornafjörður. The bridge was a 102-m-long concrete beam bridge, single-lane and with six spans. The bridge was an important link in completing the ring road, and 10 years after its construction, the road was fully connected [6]. Figure 1 shows the bridge over Steinavötn.

The span from the abutment to the first intermediate pier was 14 m on both sides and the inner spans were 18.5 m (see Figure 2). The intermediate piers rested on timber piles that went approximately five meters into the ground.

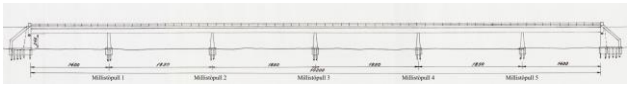

Figure 2. A view of the Steinavötn bridge from the ICRA's drawing set.

2.2 Bridge cross-section

The bridge superstructure had two different cross-sections. Four meters on either side of every pier, the cross-section was a hollow box girder shown in Figure 3. The remaining 10.5 m and 6 m in the inner and outer spans, respectively, were double T-beams illustrated in Figure 4. The bridge deck was monolithically cast and reinforced with the piers.

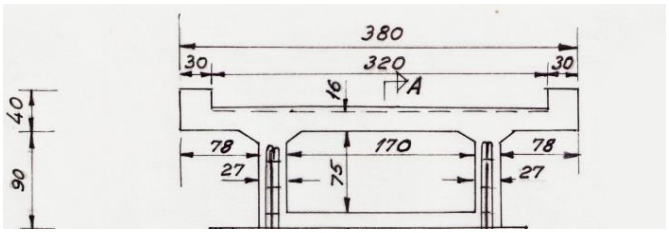

Figure 3. Bridge cross-section at pier. Hollow box girder. Measurements in cm. From the ICRA's drawing set.

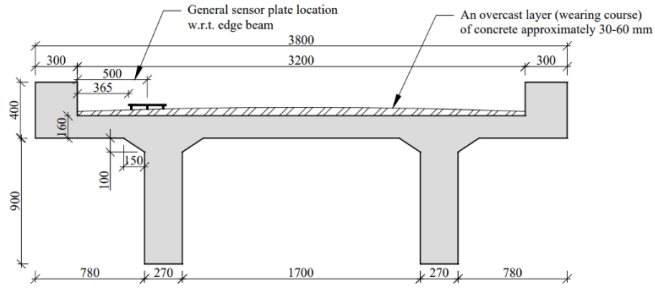

Figure 4. Bridge cross-section at midspan. Double T-beam. Measurements in mm. From the ICRA's drawing set.

2.3 Materials

Three concrete samples were extracted from the bridge using core drilling, taken from its longitudinal beams. The cylindrical samples had a diameter of 100 mm and an initial length of 270 mm, which was reduced to 200 mm by BM Vallá ehf. concrete plant, who also leveled the ends with additional concrete. The compressive strength was tested in collaboration with Mannvit hf. consulting firm following the ÍST EN 12390-3:2009 standard, applying an axial load increasing at 0.6 MPa/sec until failure. The average compressive strength was 37.7 MPa [2].

Ultra-sonic measurements were performed on the side beams of the superstructure to determine the dynamic modulus of elasticity of the concrete. The average dynamic modulus of elasticity was 39 GPa [7]. Note that the dynamic modulus can be approximately 20-30% higher than the static one [8]. According to Eurocode EC2, the static modulus of elasticity for concrete strength 37.7 MPa is 33 GPa [9]. This is 15% of the measured dynamic modules.

Three samples were taken from the longitudinal reinforcement and three from the shear reinforcement of the bridge. The steel strength was determined through tensile testing in collaboration with Mannvit, following the ÍST EN ISO 15630-1:2019 standard, with a 200 mm anchorage length at each end for proper grip. Due to challenges regarding the equipment, only the yield and ultimate strength were recorded [2].

Table 1 shows the material properties that were recorded and the values used in the subsequent analysis.

Table 1. Material properties.

Measurements				
	Compr. strength [MPa]	Dyn. E [GPa]	Yield stress [MPa]	Ultim. stress [MPa]
Concrete	37.7	39	-	-
Steel stirrup	-	-	290	439
Steel longit.	-	-	405	758
Used in analysis				
	f_{ck} [MPa]	f_{yk}/f_{uk} [MPa]	E_c [GPa]	E_s [GPa]
Concrete	38	-	33	-
Steel	-	400/760	-	210

2.4 Bridge after scour damage

In September 2017, there was a large increase in water in the river, resulting in scouring at intermediate pier 2, measured from the western end of the bridge. The settlement of the pier was measured at about 200 mm, but it also deviated and tilted by 70 mm/1000 mm, or 7%, from the vertical [1]. Figure 5 shows how the bridge pier has subsided. Cracks could be seen on the bridge superstructure above the seats of intermediate piers 1 and 3, which extended 5 m into the water. Since the bridge piers were cast and reinforced with the bridge deck, rotation of a pier therefore caused rotation of the bridge deck. Crack formations above the intermediate piers strongly indicated that floating elements had formed at these locations. After a site visit by the Icelandic Road Administration and stress tests in early October 2017, the bridge was deemed unusable [10]. Subsequently, a temporary bridge was built to allow traffic to reopen, and in September 2021, a new double-lane bridge over Steinavötn was inaugurated.

DOI: 10.3217/978-3-99161-057-1-157

Figure 5. The intermediate pillar of the bridge has sunk [10].

3 BRIDGE TESTS

This section offers a comprehensive overview of the monitoring experiments conducted on the old Steinavötn bridge during the summer and fall of 2019, prior to its demolition. The IRCA chose to utilize the bridge as an educational and research resource prior to its demolition and commenced comprehensive experiments on it in collaboration with various Icelandic and international partners. Multiple experiments were carried out on the bridge, measuring acceleration, deflection, strain, and static loading.

3.1 Short overview of tests

Figure 6 illustrates a side view of the Steinavötn bridge, highlighting the test span subjected to various structural analyses. The bridge, spanning the Steinavötn river, is depicted with five piers (labeled Pier 1 through Pier 5) and six spans (Span 1 through Span 6).

Notably, Figure 6 identifies "plastic hinge" locations in Span 1 and Span 3, indicating potential areas of structural weakness. The bridge is further divided into "Damaged Structure" and "Undamaged Structure". A note points to a pier damaged during a flood in September 2017, contributing to the "Damaged Structure" classification.

Researchers from ETH Zürich used single-axis accelerometers to measure the vertical acceleration response of the Steinavötn bridge within the test span. They installed sensors during the summer to monitor long-term ambient background vibrations and conducted damage detection experiments in September.

The OSMOS Group employed Fiber Bragg Grating sensors, including OSMOS Optical Strands, a Thermal Probe, and the OSMOS Expert Data Acquisition System, to measure strain in real-time within the test span. The sensors were installed on the bridge beams in July 2019. The sensors recorded mostly strain, but also some temperature data, evaluated through remote activation, until the ultimate load test in September 2019. The sensors were uninstalled prior to the bridge demolition.

Reykjavik University conducted two measurement campaigns on the bridge, utilizing five 3-axial accelerometers and two LVDT displacement sensors within the test span. The data from those measurements have been used to analyze the response of the bridge, and more details and results can be found in [3].

In September 2019, IRCA and Reykjavik University jointly performed a shear capacity test on the test span of the bridge, monitoring both strain and displacement.

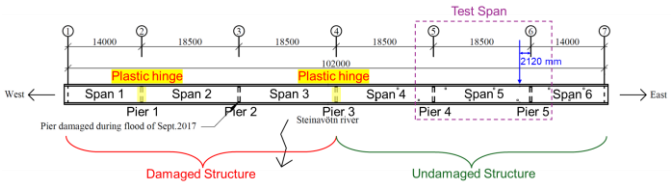

Figure 6. Side view of the Steinavötn bridge illustrating the test span (between Piers 4 and 5) used for structural analysis, including shear capacity testing.

3.2 Detailed description of incremental point load test

The purpose of this test is to assess the structural integrity and load capacity of the bridge component, specifically related to the Steinavötn bridge's shear capacity. The steel structures supporting the hydraulic jacks were designed to withstand a minimum bearing capacity of 3000 kN, considering steel availability and on-site assembly. According to a 2018 master's thesis [1], the Steinavötn bridge's local shear capacity is approximately 2200 kN. The experiment aims to validate these calculations and ensure the safety and reliability of the bridge structure under realistic loads.

Figure 7 depicts the test setup designed to evaluate the load-bearing capacity of the bridge structure. The setup utilizes two hydraulic jacks, each capable of applying a maximum force of 200 tons, which is distributed through 300x300 mm plates onto the bridge deck. These jacks are supported by a 5-meter-long HEA1000 beam, which transfers the load to HEB100 columns. The columns, in turn, are bolted to lower HEA1000 beams, which are restrained by two HEB300 beams and connected to piles via ø25 mm rebars. Each rebar pair is clamped to a single pile using UNP100 profiles and M20 bolts. Each pile group consists of four piles, approximately 11 meters deep.

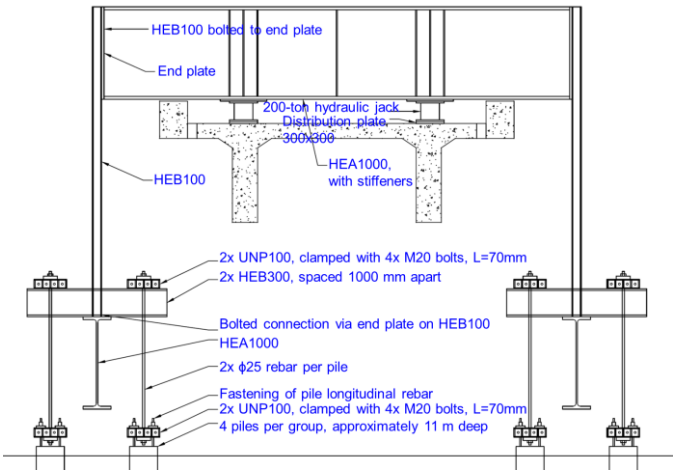

Figure 7. Test Setup

The test analyzed in this paper was performed on the 17th of September 2019. Loads were applied using the hydraulic jacks in steps, starting at approximately 500 kN and reaching approximately 2300 kN. The load as measured by the load cells is shown in Figure 8.

DOI: 10.3217/978-3-99161-057-1-157

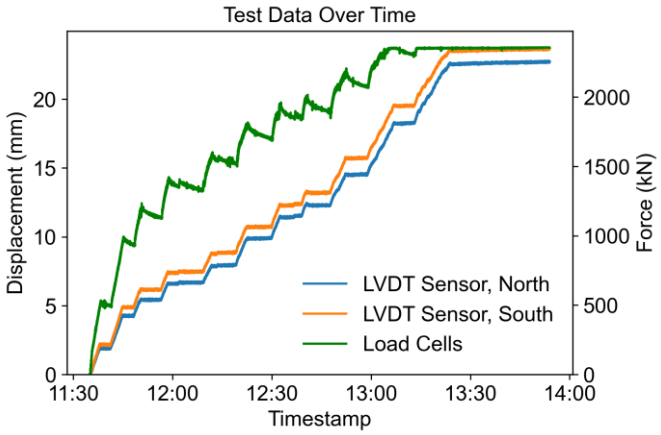

Figure 8. Displacement and force measurements during incremental point load test.

4 FIBER-OPTIC AND DISPLACEMENT SENSORS

Before the load tests were conducted, long-gauge fiber-optic strain sensors from the technology company OSMOS were installed on the bridge in axial, parallel, and crossed topologies; see Figure 9. During the incremental point load test, an LVDT sensor was placed under each T-beam in the center of the tested span.

4.1 Long-gauge fiber-optic strain sensors

Fiber-optic sensors emerged several decades after the invention of electrical strain gauges. Fiber-optic sensors are primarily made of silica, an inert material resistant to chemical exposure, and electromagnetic interference [11]. This makes silica highly suitable for measurements in harsh environments like concrete. The fiber optic serves both as the sensor and the transmission medium for the measurement. Depending on its configuration, a fiber-optic sensor can measure strain, tilt, acceleration, movement, temperature, humidity, corrosion, and more [12]. Additionally, multiple types of sensors can be linked together and transmit measurements through the same medium. Moreover, signals can be transmitted over long distances (several kilometers) without requiring electrical power [11], [13].

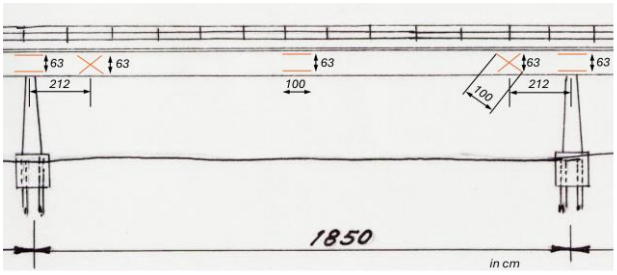

Figure 9. Long-gauge fiber-optic strain sensor locations on the south side of the monitored span. Note: sensor locations are the same on the north side of the span except lower sensors in parallel topologies over piers are not present.

Discrete strain gauges are either short (approximately 10–100 mm) or long (250–10,000 mm) [13]. Short- and long-gauge sensors provide similar results in homogeneous materials. Common construction materials, particularly concrete, are far from homogeneous, as they are characterized by aggregates, cracks, and pores [14]. The properties of concrete are thus discontinuous, and while short strain gauges can provide accurate information about localized strains, it is nearly impossible to accurately represent the overall strain state of a concrete structure with short gauge sensors. However, long gauge strain sensors measure the average strain over their gauge length, offering a better overview of the behavior in heterogeneous materials. In other words, it is often less relevant to know the strain in the individual components of concrete (cement paste, aggregates, phase boundaries) but far more relevant to measure the overall behavior and response of the material referred to as concrete. Further discussion on the accuracy and applicability of long-gauge fiber-optic strain sensors can be found in the literature, f.ex. [15], [16], [17].

Parallel strain sensors provide information about the average curvature of the cross-section [13], specifically,

$$\kappa = \frac{\varepsilon_1 - \varepsilon_2}{h} \quad (1)$$

where:
κ is the average curvature of the cross-section in $\mu\varepsilon/\text{mm}$
ε_1 is the axial strain measured by the lower sensor in a parallel topology in $\mu\varepsilon$
ε_2 is the axial strain measured by the upper sensor in a parallel topology in $\mu\varepsilon$
h is the distance between the two sensors in mm

Crossed strain sensors are intended to measure the average shear strain over the height of the cross [13], specifically,

$$\gamma = \frac{\varepsilon_1 - \varepsilon_2}{2\cos(\alpha)\sin(\alpha)} \quad (2)$$

where:
γ is the average shear strain in μrad
ε_1 is the axial strain measured by sensor 1 in the crossed topology in $\mu\varepsilon$
ε_2 is the axial strain measured by sensor 2 in the crossed topology in $\mu\varepsilon$
α is the angle between the sensors in the cross

The curvature over the east pier and shear under the load, as measured by the parallel and crossed sensors respectively, are shown in Figure 10 and Figure 11.

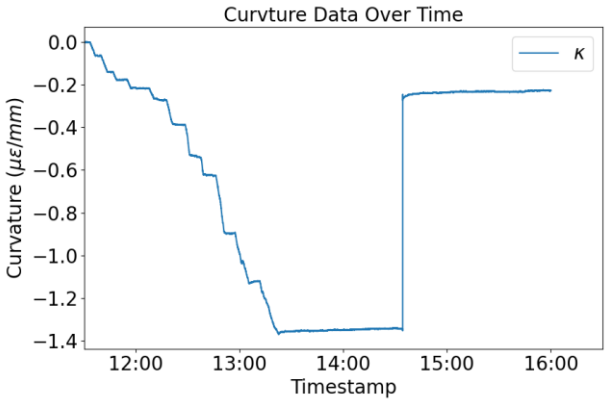

Figure 10. Average curvature over east pier during the incremental point load test.

DOI: 10.3217/978-3-99161-057-1-157

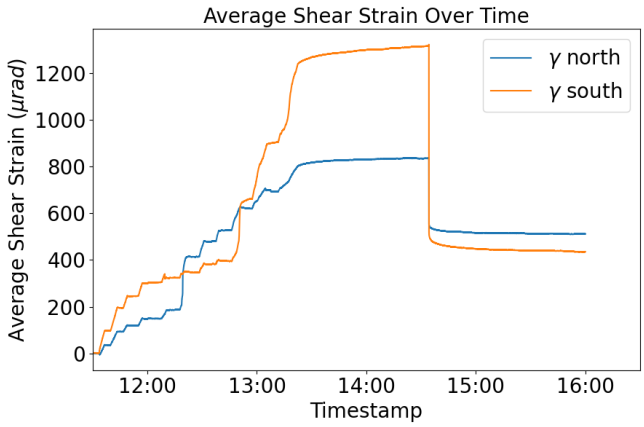

Figure 11. Average shear strain under the load during the incremental point load test.

4.2 LVDT displacement sensors

Linear Variable Differential Transformers (LVDT) are known for their precision, dependability, and adaptability in measuring linear displacement [18]. The measurements from the middle of the span during the incremental point load test are shown in Figure 8 along with the load measurements.

5 LINEAR APPROXIMATIONS

Linear approximations for deformation at midspan, curvature and shear strain are provided in the following sections. These linear approximations become increasingly inaccurate as the load increases, more cracks form, and the structural behavior becomes more nonlinear.

5.1 Deformation

The deformation is estimated using handbook equations for deformation of beams with different boundary conditions [19]. The true behavior of the span is somewhere between these two as the boundary conditions are stiffer than for the simply supported beam and softer than the fixed-fixed beam. Thus, the true deformation is a weighted average of the two equations.

Simply supported beam:

$$\Delta_x = \frac{Pbx}{6EIl}(l^2 - b^2 - x^2) \tag{3}$$

Beam with fixed-fixed supports:

$$\Delta_x = \frac{Pb^2x^2}{6EIl^3}(3al - 3ax - bx) \tag{4}$$

where:
Δ_x is the deformation at location *x* in mm.
P is the load in N
a is the location of the load from the left support in mm
b is the location of the load from the right support in mm
l is the total length of the span, $l = a + b$, in mm
E is the elastic modulus in MPa
I is the moment of inertia of the cross-section in mm^4

5.2 Curvature

When assuming linear behavior the curvature in the cross-section is

$$\kappa = \frac{M}{EI} \cdot 10^6 \tag{5}$$

where:
κ is the average curvature in $\mu\varepsilon/\text{mm}$
M is moment in the section in Nmm
E is the elastic modulus in MPa
I is the moment of inertia of the cross-section in mm^4

5.3 Shear

When assuming that the material behaves within the linear elastic range, the shear stress in a hollow box cross-section can be expressed as:

$$\gamma = \frac{VA\bar{y}}{2GIt} \cdot 10^6 \tag{6}$$

where:
γ is the average shear strain in μrad
V is the shear force acting on the section in N,
A is the area above the point where the stress is calculated in mm^2,
$\bar{y}$ is the distance from the centroid of A to the centroid of the cross-section in mm
G is the shear modulus in MPa
I is the moment of inertia of the cross-section in mm^4
t is the thickness of the web (total thickness 2t) in mm

6 NONLINEAR NUMERICAL MODELS

6.1 OpenSees

OpenSees (Open System for Earthquake Engineering Simulation) is a software framework for developing applications in earthquake engineering using finite element methods [20]. It is designed to simulate the behavior of structural and geotechnical systems subjected to earthquakes. The flexibility of OpenSees allows researchers and engineers to create customized models that can accurately reflect the unique characteristics of various materials and structural configurations. This capability makes it an invaluable tool in assessing the performance of structures during seismic events and informing design improvements.

The Beam Truss Model (BTM) proposed by Lu and Panagiotou [21] and Lu et al. [22] is a design-oriented analysis method used to model reinforced concrete (RC) structures, efficiently computing the force and deformation capacity of RC components. It represents a wall component as an assemblage of horizontal, vertical, and inclined line elements with a beam formulation and a fiber section, capturing nonlinear out-of-plane flexural resistance and its coupling with axial and in-plane flexural/shear resistance. This method makes it possible to get a more accurate picture of how the structure will behave under different loads, which makes design predictions more reliable. The BTM also makes it easier to include advanced material models, which helps engineers better understand how the different parts of reinforced concrete structures interact with each other.

There is a biaxial truss element in OpenSees called Truss2. It is meant to consider biaxial effects in a uniaxial element when it is used with the ConcretewBeta material. The ConcretewBeta material is a uniaxial concrete material model in OpenSees that considers the effect of normal tensile strain on the compressive behavior of concrete, using a tri-linear compressive stress-strain envelope to model strength degradation in tension. This interaction allows for a more accurate representation of how

DOI: 10.3217/978-3-99161-057-1-157

concrete structures respond under various loading conditions, particularly when subjected to simultaneous axial and lateral forces. By utilizing the Truss2 element with the ConcretewBeta material, engineers can better predict potential failure mechanisms and optimize the design of reinforced concrete elements for enhanced safety and performance.

6.2 OpenSees model of Steinavötn bridge

In this study, the test span of the Steinavötn bridge was modeled utilizing OpenSees with the BTM approach. The span was discretized into 60 units along its length. As illustrated in Figure 12, the blue lines, parallel to the bridge's longitudinal axis, were modeled as longitudinal elements. These dispBeamColumn elements are particularly suited for capturing nonlinear material and geometric behavior. Thirteen dispBeamColumn elements with fiber sections were used, totaling 780 elements. The fiber sections incorporated Steel02 material for rebar and Concrete04 material for concrete. Hollow boxed girder and double T-beam sections have been considered with different fiber sections at the bottom of the cross-section (this distinction is not visible in Figure 12). This fine discretization allowed for a detailed representation of the nonlinear material behavior under the incremental point load test. The red lines, representing the transverse elements of the deck, were modeled. In contrast, elasticBeamColumn elements model beams and columns with linear elastic material properties. Twelve elasticBeamColumn elements were used per cross-section, totaling 732 elements. The piers, located on both sides, were modeled with two elasticBeamColumn elements each, bringing the total number of elasticBeamColumn elements to 736. These elasticBeamColumn elements considered only the concrete's Young's modulus, assuming linear elastic behavior. The green lines, representing the diagonal elements of the triple-layer grid structure (Truss2 elements), a key component of the Beam-Truss model, totaled 1440 elements, incorporating the ConcretewBeta material to model the concrete's tensile and compressive response. The total number of elements used in the OpenSees model was 2952. Fixed boundary conditions, denoted by magenta squares in Figure 12, were applied at the base of the piers to simulate the support constraints.

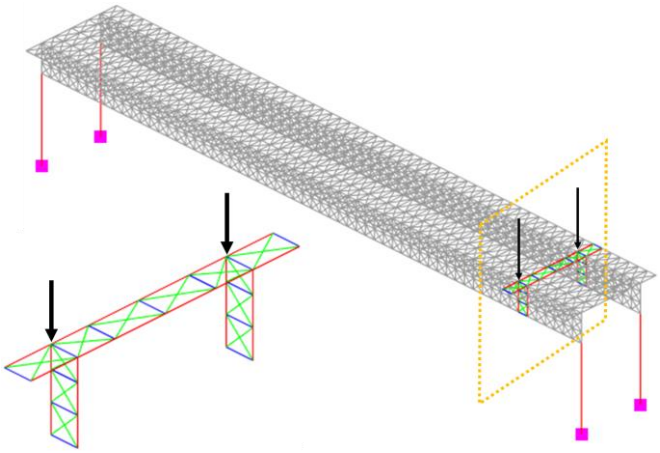

Figure 12. OpenSees model of the Steinavötn bridge with applied loads, highlighting the structural discretization.

Information on deformation is extracted directly from the midspan of the model. For evaluation of the curvature and shear, strains are extracted at the sensor locations, and the curvature and shear strain are calculated using Equations (1) and (2).

7 RESULTS

The results from measurements, linear approximations, and nonlinear numerical modelling are presented in Figure 13 to Figure 15. The results are presented as force-response diagrams highlighting the nonlinearity of the bridge behavior at high loads. The measurement results are shown in yellow and red, with measurements on the north side of the bridge in yellow and on the south side in red, the linear approximations in dot-dashed gray, and the nonlinear OpenSees results in dashed black.

The load-displacement at midspan is reported in Figure 13. The measurements fall between the linear approximations of the fixed beam and the simply supported beam, as was expected. The weighted average is calculated by combining 30% of the response from the fixed beam and 70% from the simply supported beam. However, the measured displacement is never truly linear. The nonlinear model has the same slope as the simply supported beam and starts to deviate from that line when the load reaches approximately 1500 kN. The model appears to have more capacity than the real structure.

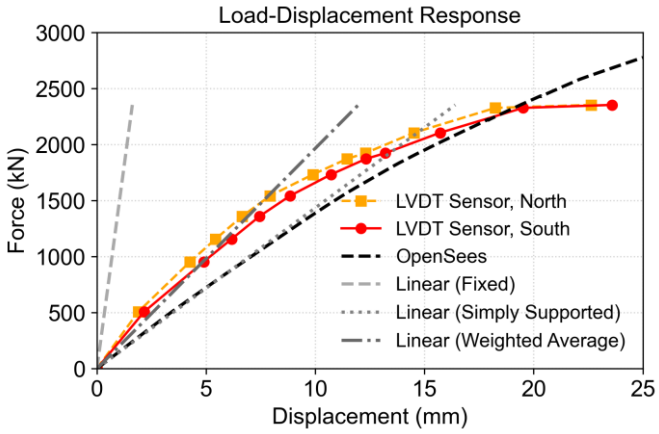

Figure 13. Load-displacement diagram. Results from measurements, linear approximations, and nonlinear numerical modelling at midspan.

The load-curvature at the east pier is shown in Figure 14. The curvature is calculated from strain measurements and nonlinear numerical modelling strains using Equation (1). The linear approximation is calculated using Equation (5). The measured curvature exhibits linear behavior very close to the linear approximation until the load reaches approximately 1500 kN. The nonlinear numerical model changes stiffness (slope) when the load reaches 500 kN and then again when the load reaches 1500 kN. The nonlinear numerical model shows less stiffness than the measurements. This is reasonable since the numerical model is a single span supported by piers, not including the adjacent spans that will increase stiffness. However, despite this minor difference in stiffness, the model successfully models the measured behavior.

DOI: 10.3217/978-3-99161-057-1-157

The load-shear strain relationship close to the east pier is shown in Figure 15. The average shear strain from fiber-optic strain measurements in crossed topologies on the north and south side of the bridge is calculated using Equation (2). The same equation is used to calculate the simulated shear strain using strains from the Truss2 element in the OpenSees model. Note that $\alpha = 45°$ in the model whereas $\alpha = 39°$ for the fiber-optic strain sensors.

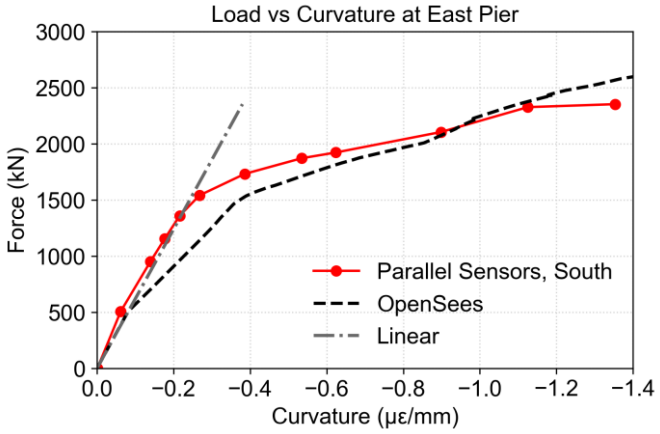

Figure 14. Load-Curvature diagram. Results from measurements, linear approximations, and nonlinear numerical modelling at the east pier.

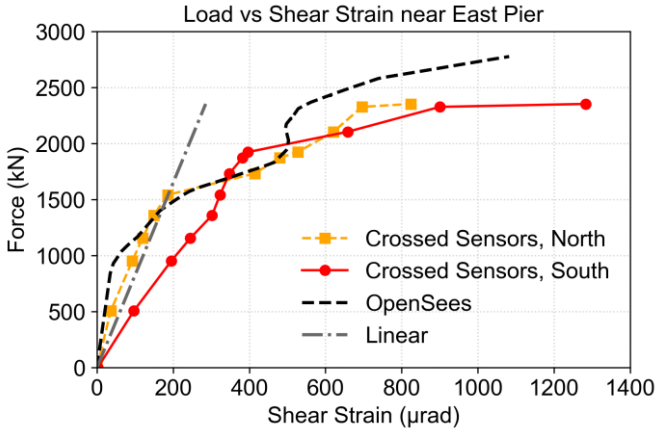

Figure 15. Load-Shear Strain diagram. Results from measurements, linear approximations, and nonlinear numerical modelling near the east pier.

In the incremental point load test the load is applied directly above the crossed fiber-optic strain sensors. The internal shear diagram for the bridge thus has a sharp discontinuity exactly at the sensor location. Additionally, according to St. Venant's principle the strain field directly under the force is heavily perturbed. However, despite these circumstances the average measured strain on the north side is in good agreement with the linear approximation until the load reaches 1500 kN. On the south side the stiffness seems to be less than on the north side and the stiffness changes before the load reaches 1500 kN. More detailed analysis is needed to explain the difference between the response on the north and south side of the bridge.

The nonlinear numerical model shows stiffer behavior under low loads than the fiber-optic measurements and changes stiffness when the load reaches 1000 kN. Generally, the numerical results are in good agreement with measurements on the north side of the bridge.

8 DISCUSSION

Simple linear approximations are able to describe the linear behavior of this concrete structure. When the load reaches 1500 kN, a nonlinear response is observed in all studied parameters. The load-displacement behavior at midspan demonstrates that measured displacements fall between the linear approximations of a fixed and simply supported beam, with an estimated weighted response of 30% fixed and 70% simply supported. While the nonlinear numerical model captures the general trend, it predicts a higher load capacity than observed in measurements.

The load-curvature relationship at the east pier exhibits good agreement between measurements and the linear approximation up to approximately 1500 kN. The nonlinear numerical model changes stiffness at 500 kN and 1500 kN and generally shows less stiffness than measured values. This difference is attributed to the model's exclusion of adjacent spans, which would otherwise contribute to the bridge's overall stiffness. Nonetheless, the nonlinear model successfully replicates the measured strain behavior at sensor locations, validating its reliability.

An important factor to keep in mind is that Equation (1) is based on the assumption that plain sections remain plain and that the strain distribution over the height of the cross-section is linear. This assumption is true in the linear elastic range of the materials, demonstrated by the excellent agreement between the linear approximation and the measurements. However, after the materials enter the nonlinear regime, plain sections do not necessarily remain plain and the assumption that the strain varies linearly between the two parallel sensors is not necessarily correct. In other words, the slope of the line between the two strain measurements in the parallel sensor topology does not necessarily accurately describe the curvature of the cross-section when the bridge starts to behave nonlinearly. The fact that the curvature obtained by this method from the strain measurements and the nonlinear model are similar demonstrates that nonlinear model successfully simulates the strains at the sensor locations.

The load-shear strain relationship near the east pier reveals a strong correlation between measured strains and the linear approximation up to 1500 kN on the north side. However, the south side exhibits lower stiffness and an earlier stiffness change, necessitating further investigation to understand these discrepancies. The nonlinear numerical model shows higher stiffness at low loads and a change in stiffness at 1000 kN but aligns well with measurements on the north side. Strains as simulated by the nonlinear OpenSees model are similar to the measurements from strain sensors, resulting in curvature and shear strain with similar behavior. This result highlights the strength of the Truss2 elements in OpenSees in conjunction with crossed fiber-optic sensors.

DOI: 10.3217/978-3-99161-057-1-157

9 CONCLUSION

This paper presents the Steinavötn bridge that was damaged during flooding in 2017. Subsequently, before demolition, the bridge was instrumented with long-gauge fiber-optic strain sensors and LVDT sensors, and tests carried out far into the nonlinear regime. This paper presents the load-response behavior of the bridge under the incremental point load test using the fiber-optic and LVDT measurements, linear approximations, and nonlinear numerical modeling in OpenSees.

The analyzed parameters were displacement at midspan, curvature at the east pier and shear strain near the east pier (under the load). All analyzed parameters exhibit linear behavior up to an approximate load of 1500 kN. The results highlight the bridge's nonlinear response at high loads and provide valuable insights into its structural behavior.

More in depth analysis of the nonlinear strain field from the OpenSees model is necessary to evaluate the error caused by the linear assumptions made in the data analysis of the sensor and numerical data. Overall, the nonlinear numerical model effectively captures key aspects of the bridge's nonlinear response, despite minor discrepancies in stiffness predictions.

Future research should focus on refining the numerical model, exploring differences between the north and south side responses, and evaluating the effects of adjacent spans to enhance predictive accuracy.

ACKNOWLEDGMENTS

Funding from the Icelandic Road and Coastal Administration (IRCA) research fund (grant no. 1800-1068) is gratefully acknowledged, as is the cooperation with IRCA staff members, E. Óskarsson and Ó. S. Haraldsson. Also, thanks to OSMOS staff and J. Snæbjörnsson at Reykjavik University.

REFERENCES

[1] H. Bogason, "Tjónagreining á brúnni yfir Steinavötn í Suðursveit," MS, Unversity of Iceland, Reykjavík, 2018.

[2] A. G. Ragnarsson, "Burðarþolsrannsókn á brú yfir Steinavötn í Suðursveit," BSc, Reykjavik University, Reykjavík, 2020.

[3] Þ. V. Jónasdóttir, "The Steinavötn Bridge (translated: Steinavotn Broen)," Master Thesis, DTU, 2021.

[4] T. Jonasdottir, J. Snæbjörnsson, and R. Brincker, "Modelling a Damaged Multi-span RC Bridge Based on Structural Monitoring Data," 2023, pp. 134–143. doi: 10.1007/978-3-031-07258-1_15.

[5] Þ. J. Tryggvason, "Ólínuleg töluleg greining á brotmörkum steinsteyptrar brúar yfir Steinavötn," MS, Unversity of Iceland, Reykjavík, 2023.

[6] Vegagerðin, "Brýr og vegur yfir Skeiðarársand, 40 ár frá opnun lokaáfanga Hringvegarins," *Framkvæmdaféttir*, vol. 22, no. 16, Jul. 2014.

[7] Þ. V. Jónasdóttir and J. Þ. Snæbjörnsson, "Structural analysis and modelling of a reinforced concrete bridge based on full scale data," Reykjavík, 2021.

[8] W. de A. Thomaz, D. Y. Miyaji, and E. Possan, "Comparative study of dynamic and static Young's modulus of concrete containing basaltic aggregates," *Case Studies in Construction Materials*, vol. 15, Dec. 2021, doi: 10.1016/j.cscm.2021.e00645.

[9] European Committee for Standardization, "Eurocode 2: Design of concrete structures - Part 1-1: General rules and rules for buildings," 2004, *Staðlaráð Íslands*.

[10] G. V. Guðmundsson, Ó. Einar, Ó. S. Haraldsson, A. Bjarnason, and A. G. Ragnarsson, "Burðargetumat steyptra brúa Álagsprófun brúar á Steinavötn," 2019.

[11] E. Udd and W. B. Spillman Jr., *Fiber optic sensors. An introduction for engineers and scientists*, 2nd ed. Hoboken, New Jersey, USA.: Wiley, A Johan Wiley & Sons, Inc., Publication, 2011.

[12] R. M. Measures, *Structural monitoring with fiber optic technology*. San Diego, USA.: Academic Press; A Harcourt Science and Technology Company, 2001.

[13] B. Glisic and D. Inaudi, *Fibre optic methods for structural health monitoring*. Chichester, England: John Wiley & Sons Ltd, The Atrium, Southern Gate, 2007.

[14] J. F. Young, S. Mindess, R. J. Gray, and A. Bentur, *The science and technology of civil engineering materials*. Upper Saddle River, New Jersey, USA: Prentice Hall, International Series in Civil Engineering and Engineering Mechancis, 1998.

[15] B. Glisic, "Influence of the gauge length on the accuracy of long-gauge sensors employed in monitoring of prismatic beams," *Meas Sci Technol*, vol. 22, no. 3, 2011.

[16] D. H. Sigurdardottir, J. Stearns, and B. Glisic, "Error in the determination of the deformed shape of prismatic beams using the double integration of curvature," *Smart Mater Struct*, vol. 26, no. 7, 2017, doi: 10.1088/1361-665X/aa73ec.

[17] D. H. Sigurdardottir and B. Glisic, "Detecting minute damage in beam-like structures using the neutral axis location," *Smart Mater Struct*, vol. 23, no. 12, 2014, doi: 10.1088/0964-1726/23/12/125042.

[18] A. Sivasuriyan *et al.*, "Emerging Trends in the Integration of Smart Sensor Technologies in Structural Health Monitoring: A Contemporary Perspective," Dec. 01, 2024, *Multidisciplinary Digital Publishing Institute (MDPI)*. doi: 10.3390/s24248161.

[19] B. Chr. et al. Jensen, *Teknisk Ståbi*, 19th ed. Copenhagen: Nyt Teknisk Forlag, 2007.

[20] F. McKenna, G. L. Fenves, M. H. Scott, and B. Jeremic, "OpenSees," 2000, *Berkeley, Univ. of California*: 2.3.2.

[21] Y. Lu and M. Panagiotou, "Three-Dimensional Cyclic Beam-Truss Model for Nonplanar Reinforced Concrete Walls," *Journal of Structural Engineering*, vol. 140, no. 3, Mar. 2014, doi: 10.1061/(ASCE)ST.1943-541X.0000852.

[22] Y. Lu, M. Panagiotou, and I. Koutromanos, "Three-dimensional beam-truss model for reinforced concrete walls and slabs – part 1: modeling approach, validation, and parametric study for individual reinforced concrete walls," *Earthq Eng Struct Dyn*, vol. 45, no. 9, pp. 1495–1513, Jul. 2016, doi: 10.1002/eqe.2719.